



**HAL**  
open science

## **Deciphering the exceptional preservation of the Early Triassic Paris Biota (Bear Lake County, Idaho, USA).**

Miguel Iniesto, Christophe Thomazo, Emmanuel Fara, Arnaud Brayard, Kevin G. Bylund, Gilles Escarguel, Nicolas Goudemand, Pierre Guériau, James F. Jenks, Laurel J. Krumenacker, et al.

### ► **To cite this version:**

Miguel Iniesto, Christophe Thomazo, Emmanuel Fara, Arnaud Brayard, Kevin G. Bylund, et al.. Deciphering the exceptional preservation of the Early Triassic Paris Biota (Bear Lake County, Idaho, USA).. *Geobios*, 2019, 54, pp.81-93. 10.1016/j.geobios.2019.04.002 . hal-02168504

**HAL Id: hal-02168504**

**<https://hal.science/hal-02168504>**

Submitted on 25 Oct 2021

**HAL** is a multi-disciplinary open access archive for the deposit and dissemination of scientific research documents, whether they are published or not. The documents may come from teaching and research institutions in France or abroad, or from public or private research centers.

L'archive ouverte pluridisciplinaire **HAL**, est destinée au dépôt et à la diffusion de documents scientifiques de niveau recherche, publiés ou non, émanant des établissements d'enseignement et de recherche français ou étrangers, des laboratoires publics ou privés.



Distributed under a Creative Commons Attribution - NonCommercial 4.0 International License

## **Deciphering the exceptional preservation of the Early Triassic Paris Biota (Bear Lake County, Idaho, USA) <sup>★</sup>**

Miguel Iniesto <sup>a,b,\*</sup>, Christophe Thomazo <sup>a</sup>, Emmanuel Fara <sup>a</sup>, the Paris Biota Team <sup>†</sup>

<sup>a</sup> Biogéosciences UMR 6282, CNRS, Université Bourgogne Franche-Comté, 6 Boulevard Gabriel, 21000 Dijon, France

<sup>b</sup> Laboratoire Ecologie Systématique Evolution, CNRS, Université Paris-Sud, AgroParisTech, Université Paris-Saclay, Orsay, France

<sup>†</sup> The Paris Biota Team includes, in alphabetical order: Arnaud Brayard (team leader; Biogéosciences, Univ. Bourgogne Franche-Comté, Dijon, France), Kevin G. Bylund (Spanish Fork, UT, USA), Gilles Escarguel (LEHNA, Univ. Lyon 1, Lyon, France), Emmanuel Fara (Biogéosciences, Univ. Bourgogne Franche-Comté, Dijon, France), Nicolas Goudemand (IGFL, ENS-Lyon, Lyon, France), Pierre Gueriau (Synchrotron SOLEIL, Gif-sur-Yvette, France/Institute of Earth Sciences, University of Lausanne, Swiss), James F. Jenks (West Jordan, UT, USA), L.J. Krumenacker (Idaho Museum of Natural History, Idaho State Univ., Pocatello, ID, USA), Nicolas Olivier (Magmas et Volcans, Univ. Clermont Auvergne, Clermont-Ferrand, France), Daniel A. Stephen (Dpt. of Earth Sciences, Utah Valley Univ., Orem, UT, USA), Christophe Thomazo (Biogéosciences, Univ. Bourgogne Franche-Comté, Dijon, France), Mathieu Thoury (IPANEMA, Univ. Paris-Saclay/Synchrotron SOLEIL, Gif-sur-Yvette, France), and Emmanuelle Vennin (Biogéosciences, Univ. Bourgogne Franche-Comté, Dijon, France).

\* Corresponding author. E-mail address: [miguel.iniesto@gmail.com](mailto:miguel.iniesto@gmail.com) (M. Iniesto).

<sup>★</sup> Corresponding editor: Arnaud Brayard.

### **Abstract**

After the end-Permian mass extinction, the Early Triassic (~251.9 to 247 Ma) is characterized by several biotic crises that particularly affected marine faunas;

accordingly, marine ecosystems from this unstable interval have been often described as heavily depauperate. This assumption, however, may relate to a biased fossil record. The discovery of taphonomic windows, like *Konservat-Lagerstätten*, in the Early Triassic would help to better understand the composition and diversity of ecosystems at that time. The Paris Biota (Idaho, USA) is a highly diverse fossil assemblage from the earliest Spathian (middle Olenekian, ~250.6 Ma), indicating a rapid rediversification for many groups after the end-Permian crisis and pointing toward a remarkably complex marine ecosystem ~1.3 m.y. after the Permian-Triassic boundary. However, its detailed taphonomy has not yet been investigated. Here we present the mineral characterization of four of its most abundant taxa: discinoid and linguloid brachiopods, leptomitid sponges, and caridean shrimps. For this purpose, we combined data from Raman microspectroscopy, Fourier Transform InfraRed spectroscopy, and SEM-EDXS. Although all taxa were preserved in calcium phosphate, the morphology, structuring and size of crystals are highly dissimilar at a nano- to micrometric scale. In brachiopods, the ultrastructure of calcium phosphate shows unorganized bacillary-like crystals, while in crustaceans their size is considerably smaller and round-shaped. Similar small crystals are observed in sponges. However, the ultrastructure of calcium phosphate in sponges exhibits a well-defined preferential orientation. In addition, sponges show some compressed but preserved three-dimensional features, with an inner surface better preserved. Such analyses are essential to understand the taphonomic pathways enabling exceptional preservation. The further comprehension of preservation features would help to understand potential bias on observed diversity signals and their interpretation.

*Keywords:*

Paris Biota

Early Triassic

Taphonomy

Fossil characterization

Raman microspectroscopy

Fourier-transform infrared spectroscopy

## **1. Introduction**

The biotic crisis at the Permian-Triassic (PT) boundary (~251.9 Ma) was the most severe Phanerozoic mass extinction (Raup, 1979). Subsequent environmental conditions during the Early Triassic were portrayed as unstable, with recurrent changes in water temperature (Sun et al., 2012; Romano et al., 2013), large-scale fluctuations of the global carbon cycle, and harsh marine conditions including a combination of ocean acidification, euxinia and fluctuating productivity (Payne et al., 2004; Galfetti et al., 2007; Grasby et al., 2013). Associated with this catastrophic scenario, marine benthic ecosystems have frequently been assumed as heavily depauperate in diversity, showing a delayed and spatio-temporally heterogeneous recovery (Beatty et al., 2008; Hofmann et al., 2014; Foster et al., 2015). In contrast with this delayed recovery scenario, an exceptionally well-preserved and complex Early Triassic marine biota from Paris Canyon (Bear Lake County, south-eastern Idaho, USA) has been described recently (Brayard et al., 2017). The occurrence of the ammonoid *Tirolites harti* Smith, 1932 indicates an early Spathian age (middle Olenekian, ~250.6 Ma, i.e., only ~1.3 m.y. after the PT boundary) for this biota (Brayard et al., 2019b). Therefore, it constitutes the oldest Early Triassic complex marine ecosystem known so far. The existence of this *Konservat-Lagerstätte*, i.e., deposits with exceptional preservation of fossils (Seilacher, 1970), is all the more surprising as it immediately follows a second severe extinction at the end of the Smithian (Orchard, 2007; Brayard et al., 2009; Jattiot et al., 2016). This crisis and its aftermath are associated in the sedimentary record with major perturbations of the global biogeochemical cycles (Payne and Clapham, 2012), although some local diagenetic phenomena have probably contributed to modify this signal (Thomazo et al., 2016, in press). This period is also characterized by successive rises and drops of seawater temperature (Romano et al., 2013). The discovery of an ecosystem as diverse as the Paris Biota was thus highly unexpected (Brayard et al., 2017; Doguzhaeva et al., 2018). On that ground, an understanding of the chemical processes leading to its exceptional preservation is the aim of this study.

The fossil assemblage of the Paris Biota (PB) represents a diverse marine ecosystem with a remarkable richness and abundance of sponges, brachiopods, echinoderms, cephalopods, arthropods and vertebrate remains. These fossils represent at least seven phyla and more than 20 orders, which indicate higher survival and post-PT diversification rates than previously expected after the PT crisis and in the immediate wake of the end-Smithian event, at least for several groups (Brayard et al.,

2017, 2019b; Doguzhaeva et al., 2018; Charbonnier et al., 2019; Romano et al., 2019; Saucède et al., 2019; Thuy et al., 2019). In addition, interest in the PB is enhanced by the occurrence of highly unexpected taxa. Indeed, it combines early Paleozoic and middle Mesozoic taxa previously unknown from any Triassic strata. Among those, usually Cambrian-Ordovician leptomitid sponges (a ~200-m.y. Lazarus taxon; Brayard et al., 2017; Botting et al., 2019) co-occur with gladius-bearing coleoids, a group that was hitherto poorly documented before the Jurassic (~50 m.y. after the Early Triassic; Doguzhaeva et al., 2018).

Fossils of the PB are flattened but sometimes preserve three-dimensional features. Preliminary taphonomic data, notably the frequent occurrence of articulated echinoderm and crustacean specimens, suggested a rapid entombment close to the original habitat, and no evidence of microbial mat-enhanced preservation was found (Brayard et al., 2017). This exceptional preservation of carcasses would be the result of fine sedimentation and changes in sedimentation rate (Seilacher et al., 1985). In addition, the occurrence of small framboidal and polyhedral pyrite suggests anoxic conditions in the uppermost layers of the sediment (Wang and Morse, 1996), but oxygenated bottom waters can be inferred from the abundance in the PB of benthic organisms such as ophiuroids and crinoids.

The PB represents a relevant *Konservat Lagerstätte* since it provides novel information about Early Triassic macroevolution and taphonomic processes. However, field observations and a thorough study of the fossil record should be complemented by taphonomic investigations. In fact, experimental taphonomy is an increasingly important field, essential for the correct interpretation of the fossil record. Laboratory experiments were crucial to identify several taphonomic pathways that can be involved in exceptional preservation such as:

- the effect of cell autolysis in the different tissues of the carcasses (Raff et al., 2006, 2008; Butler et al., 2015);
- selective mineralization (Briggs and Kear, 1993; Hof and Briggs, 1997; Sansom et al., 2010; Sansom, 2016; Wilson et al., 2016);
- the presence of microbial communities and their interaction with carcasses (Martin et al., 2005; Raff et al., 2013; Iniesto et al., 2013, 2015, 2017);
- diagenetic factors like increasing temperature and/or pressure (Gupta et al., 2007, 2006; Gupta, 2011; Bernard et al., 2010, 2015).

However, the relationships among these processes remain unknown. In the particular case of the PB, Brayard et al. (2017) report different types of mineralization. While belemnoid hooks are preserved as carbonaceous structures, most of the fossils such as sponges, arthropods, brachiopods and coprolites are preserved in calcium phosphate. However, their mineralogical and taphonomic characterization at a microscopic scale remains to be done. Here we describe the preservation of PB brachiopods (discinoids and linguloids), caridean shrimps, and leptomitid sponges by means of different imaging and spectroscopic techniques at the microscopic scale. These groups have been selected for two main reasons: (i) they show high abundances in the PB, and (ii) some of them had initially a mineralized shell (brachiopods), whereas others had an organic (i.e., proteinaceous and/or polysaccharidous) exoskeleton (shrimps and sponges). Comparison between these two cases will help determining the potential influence of these differences for preservation. In addition, sediment composition and mineralogy was also characterized in order to determine their potential effect on the preservation of the PB taxa.

## **2. Material and methods**

A total of 30 specimens from the PB were analysed, including 10 leptomitid sponges, 5 caridean shrimps, 5 lingulids, and 10 discinoids. All the specimens studied here are housed at the Université Bourgogne Franche-Comté, Dijon, France (Table 1). Fossils were selected randomly within the available samples and are representative of their taxa. The mineralogy of fossils was determined by scanning electron microscopy (SEM) coupled with an energy dispersive X-ray spectrometry (EDXS) detector, Raman microspectroscopy, and Fourier transform infrared spectroscopy (FTIR). In addition, the sediment forming the matrix of 5 fossils was also characterized by SEM-EDXS and X-ray diffraction (XRD) (Table 1).

### *2.1. Scanning electron microscopy and energy dispersive X-ray spectrometry*

For electron microscopy analyses, samples were coated with carbon. Images were collected in backscattered and secondary electron modes using a JEOL JSM6400F operating at 5 kV, with a 60  $\mu\text{m}$  aperture at a working distance of  $\sim 5$  mm. Analyses were performed at a distance of  $\sim 15$  mm and 15 kV. Elemental compositions were determined using energy dispersive x-ray spectrometry (EDXS) with an Oxford

Instruments detector. EDXS maps were processed using the software INCA-Energy v. 2.1 (Oxford Instruments). SEM imaging and EDXS analyses were performed at the ARCEN platform, Institut Carnot de Bourgogne (Université Bourgogne Franche-Comté, Dijon, France).

## *2.2. X-ray diffraction (XRD), Raman microspectroscopy and micro-Fourier transform infrared (micro-FTIR)*

Fresh slabs of sediment were kept overnight at 37°C in an oven and dry-crushed in a mortar until obtaining a homogeneous powder. XRD measurements were performed using the Cu K $\alpha$  radiation (1.54056 Å) on a D4 Endeavor-Bruker diffractometer. Data were recorded over a 2-65° (2 $\theta$ ) range with a step of 0.04° and a counting time of 0.5 h per sample. XRD was performed at the Biogéosciences Laboratory (Université Bourgogne Franche-Comté, Dijon, France).

Rationale for Raman analyses in taphonomic studies can be found in Beyssac et al. (2003) and Bernard et al. (2008). Raman microspectroscopy was performed with a Renishaw InVIA Reflex microspectrometer, using a 514 nm wavelength of a 50 mW Modulaser Argon laser (green laser). The spectrometer was calibrated with silicon standard. The laser was focused through a Leica DMLM microscope with a 50 $\times$  objective (NA = 0.55), and the laser power at the sample surface was set around 1 mW. Moreover, 7 fossils (2 sponges, 2 discinoids, 2 linguloids and 1 shrimp) were embedded in epoxy resin and polished with diamond paste down to  $\frac{3}{4}$   $\mu$ m in size in order to obtain thin sections, which were useful to perform Raman without sediment interference. Raman microspectroscopy was performed at the Institut de minéralogie, de physique des matériaux et de cosmochimie, Université Pierre et Marie Curie, Paris, France.

$\mu$ -FTIR analyses were performed on not-embedded samples of leptomitid sponges, caridean shrimps and linguloid and discinoid brachiopods using a Bruker Lumos  $\mu$ -FTIR microspectrometer with ZnSe beam splitter, DTGS detector and high-pressure diamond ATR. A reference background spectrum (T<sub>0</sub>) was first measured at a place away from the sample, and then transmission IR spectrum of sample (T) was measured. The IR spectrum is described as IR absorbance ( $\text{abs} = -\log_{10} T/T_0$ ) as a function of the wavenumber ( $\text{cm}^{-1}$ ). Spectra were acquired from 600 to 4000  $\text{cm}^{-1}$ .  $\mu$ -FTIR was performed at the Institut de Chimie Moléculaire, Université Bourgogne Franche-Comté, Dijon, France.

Identification of peaks in spectra obtained using Raman and FTIR spectroscopy was realized with references from the ruff database (<http://rruff.info>) (Raman: hydroxyapatite ID R050512 and fluorapatite ID R050274;  $\mu$ -FTIR: hydroxyapatite ID R050512 and calcite ID R040070).

### 3. Results

#### 3.1. Mineralogy of the PB sedimentary matrix

SEM-EDXS and XRD analyses were combined to identify the major mineral phases forming the matrix of individual fossils (Fig. 1). EDXS and the subsequent hyperspectral elemental map show two major components, with sampled spots dominated by Ca-rich zones and other zones with the co-occurrence of Si and Al/K/Mg elements (Fig. 1(A-G)). This is consistent with data from XRD (Fig. 1(H)) showing that calcite (with main XRD peaks at 3.035, 2.095 and 2.285 Å) appears as one of the most abundant phase together with Si-rich minerals: quartz ( $\text{SiO}_2$ ), with XRD peaks at 3.342, 4.257 and 1.8179 Å), illite ( $(\text{K,H}_3\text{O})(\text{Al,Mg,Fe})_2(\text{Si,Al})_4\text{O}_{10}[(\text{OH})_2,(\text{H}_2\text{O})]$ ), with peaks at 4.430, 2.560 and 3.660 Å), and albite ( $\text{NaAlSi}_3\text{O}_8$ , with peaks at 3.176, 3.211 and 4.052 Å). Finally, a phyllosilicate belonging to the chlorite group (XRD peaks at 14.055, 7.051 and 2.834 Å) was also identified.

#### 3.2. Mineralogical and ultrastructural description of the fossils

##### 3.2.1. Brachiopods

SEM observations provided information on the overall preservation of discinoids (Fig. 2(A-I)) and linguloids (Fig. 2(J-M)). For instance, preservation of the original concentric annuli in discinoid specimens is conspicuous (Fig. 2(B), arrow), whereas some others preserve these annuli only as an impression in the sediment (Fig. 2(D)). These impressions are noticeable when several parts of the shell were lost during diagenesis *sensu lato*. Figure 2(E-I) shows a 150  $\mu\text{m}$ -width of a discinoid shell being replaced by carbonates (arrow). In contrast, the integrity of the linguloid shells is remarkable and these shells are less fragmented. Linguloid brachiopod shells also preserve their growth increments (Fig. 2(J-L)). Several black spots scattered all over linguloid specimens are also visible (Fig. 2(M), arrows). These are interpreted as slot-like pits (Cusack et al., 1999) according to their distribution and number. Despite the

remarkable preservation, the expected chitinoproteinaceous layer for these brachiopods was not observed and only the original mineralized part of the shells is preserved.

EDXS-maps of Ca, Si and P show the potential occurrence of calcium phosphate in discinoid and linguloid brachiopods (Fig. 3(A-E) and (F-I), respectively). The presence of calcium phosphate was determined using  $\mu$ -FTIR spectroscopy. The  $\mu$ -FTIR spectra of both groups show the occurrence of calcite and hydroxyapatite (HAP) (Fig. 3(K)). The presence of calcite is interpreted as interference from the carbonate-rich matrix beneath the fossils. Raman spectroscopy was used in order to further characterize the HAP phase. In the case of discinoid brachiopods, we compared Raman spectra with reference spectra for hydroxyapatite. The relevant peaks that correspond to stretching and bending modes of the phosphate group are observed (Fig. 4(B); Table 2). Since we detected the presence of fluorine with EDXS (Fig. 4(A)), we also compared our results to the fluorapatite reference spectrum. Despite the presence of fluorine, the Raman spectra of the samples show a better fit with the reference spectrum of HAP, or even chlorapatite, when compared to the fluorapatite spectrum according to the  $\nu_2$  hydroxyapatite vibration (peak 1 in Fig. 4). Raman microscopy did not reveal any evidence for phosphate in linguloids, probably because of their low degree of mineralization.

### 3.2.2. Caridean shrimps

Caridean specimens seem complete and articulated when observed under UV light (Fig. 5(A); Brayard et al., 2017). However, SEM analyses well show that parts of the exoskeleton are missing (Fig. 5(B)) and that remaining parts exhibit a porous mineralized structure (Fig. 5(C, D), arrows). EDXS-maps show the co-occurrence of Ca and P (Fig. 5(E-I)). The presence of calcium phosphate was confirmed using  $\mu$ -FTIR spectroscopy (Fig. 5(J), purple arrows). However, Raman analyses did not detect calcium phosphate. In contrast, they revealed the incidence of unexpected peaks in the region of 1100-1600  $\text{cm}^{-1}$  (Fig. 6). A comparison with the signal from the sediment matrix helps to exclude any interference with the surrounding silicate and carbonate phases.

### 3.2.3. Leptomitid sponges

Sponge specimens (Fig. 7(A)) show the exceptional preservation of the external surface as a layered three-dimensional structure (Fig. 7(B)). In areas in which the

uppermost layer has been removed (black arrows), the inner layer appears as better preserved and less porous (white arrow). In addition, observations at higher magnifications ( $\times 5.000$  and  $\times 20.000$ ) reveal the absence of substantial damages in terms of ultrastructure of the inner layer (Fig. 7(C, D)). Elemental EDXS-maps show the occurrence of calcium and phosphate (Fig. 7(E-I)). As in the case of brachiopods and caridean shrimps, the FTIR signal of the calcite-rich matrix overlaps with that of the fossil but shows a distinctive calcium phosphate signature (Fig. 7(J)). Here again, the identification of HAP using Raman microscopy was unsuccessful.

In addition, two leptomitid sponge fossils exhibit a coating made by a mineral rich in sulphur and barium (Fig. 8(A-E)). This precipitate also fills the surface cracks of fossil sponges (Fig. 8(F-H)). This Ba-rich mineral phase was identified as barite ( $\text{BaSO}_4$ ) using Raman (Fig. 8(I)).

### *3.3. Ultrastructure of calcium phosphate in relation to taxonomy*

Despite similarities in calcium phosphate composition, inter-group comparisons of fossils revealed differences in organization and size of the crystals of calcium phosphate. In discinoid brachiopods, rod-shaped structures with sharp corners ( $\sim 400$  nm length) do not exhibit any preferential orientation (Fig. 9(A-C)). Moreover, mineral ultrastructure exhibits an organization in amorphous aggregates (Fig. 9(B)). In leptomitid sponges, well-preserved and bacillary-shaped rods are significantly smaller ( $\sim 100$  nm length) and, in contrast with discinoid brachiopods, display a preferential orientation following the sponge longitudinal axis (Fig. 9(G-I)). Finally, the ultrastructure of calcium phosphate crystals in caridean shrimps and linguloids is intermediate between the two end-members described above (Fig. 9(D-F)). Their size is similar to crystals found in sponges ( $\sim 100$  nm length) but they seem to be composed of amorphous small rounded aggregates (zone highlighted with a dotted circle on Fig. 9(F)). Calcium-phosphate did not show a preferential long-axis orientation as in sponges and the ultrastructure shows a twisted pattern of crystals (Fig. 9(D, E), dotted lines).

## **4. Discussion**

### *4.1. Observed differences among taxa*

All studied groups of the PB have been preserved in calcium phosphate. The absence of Raman signal in both shrimps and sponges could be explained by a lower

grade of mineralization. Morphology and organization of this mineral are dissimilar at a nanometric scale. This includes mineral size, shape and orientation (see above, Section 3.3). Such a clade-dependent feature can be explained by differences in the decay process resulting from the composition of original tissues, the associated rate of decomposition and the ensuing microenvironments. The influence of the original tissue composition in preservation processes has been extensively discussed (Briggs and Kear, 1993; Hof and Briggs, 1997; Clements et al., 2017). However, the impact of these biotic parameters on crystallization and mineral nanostructure remains unknown. In PB fossils, mineralogical dissimilarities (size and organization of crystals) can be explained by original differences, such as kinetic of calcium phosphate mineralization, presence of nucleation centres and the early pathways of mineral precipitation. Nowadays, discinoid and linguloid brachiopods have a mainly phosphatic mineralized shell and their structure correspond to what is observable on the PB specimens (Fig. 2; see Williams et al., 1998: figs. 6, 15 for discinoids, and Zabini et al., 2012: figs. 3, 5 for linguloids). Hence, calcium phosphate in discinoid fossils from the PB can be explained by the good preservation of the initial biomineral. The absence of a preferential organization and the rod-shaped structures built by smaller spherules in discinoid specimens (Fig. 9) are two features consistent with observations made on modern and fossil discinoids from different ages (Williams et al., 1998). This supports the hypothesis of a preservation of the original calcium phosphate with only weak alterations in discinoids. Mineralogical Transmission Electron Microscopy analyses of modern discinoid shells show the occurrence of amorphous/poorly-crystallized phosphates (Griesshaber et al., 2009), which is in agreement with our SEM observations and spectroscopy data (Figs. 2, 4). Differences in ultrastructure documented between discinoids and linguloids can result from the compositional differences and the number of layers in the shell (Williams et al., 1998). For instance, the highest concentration in shell pores noticed in PB linguloid specimens is consistent with modern and other fossil linguloids (Zabini et al., 2012: fig. 3) and they are not the result of decay and/or diagenetic damage. According to Balthasar (2007), the spherical pores that generate this porosity were originally occupied by a calcitic shell material but were lost during the early decay of tissues and/or the diagenetic history.

Leptomitid sponges, which are probably phylogenetically close to demosponges (Rigby and Collins, 2004; Botting et al. 2013; Muir et al. 2013; Botting, 2016), likely had

organic tissues initially containing complex polymers such as chitin within a protein matrix (Brunner et al., 2009; Ehrlich et al., 2010). Consequently, their fossilization in calcium phosphate can result from phosphatization during early decay. This type of exceptional phosphatization of organic structures during early decay has been achieved in the laboratory (Briggs and Kear, 1993; Sagemann et al., 1999). The recalcitrant organic molecules (i.e., the most chemically stable and hard to decay) forming the external part of leptomitid sponges could likely resist the initial decay and were later replicated in phosphates, maybe retaining the potential original orientation of protein fibres. This process would be analogous to the mineralization of a scaffold composed of proteins as observed in bones, where HAP maintains the orientation of the organic support (Mahamid et al., 2008, 2010). Such a taphonomic process was apparently also involved in the mineralization of the PB caridean shrimp carcasses. The lack of preferential alignment of phosphate crystals can result either from the absence of this organization in the chitin-associated proteins of the crustaceans, or from a different decay sequence influencing the mineralization. The outer layers of the shrimp exoskeleton are characterized by regular twisted planes (i.e., the Bouligand structures; Bouligand, 1965) which are responsible for enhancing carapace toughness (Zimmermann et al., 2013). While the inner layer can show a preferential orientation of chitin fibres, the outer parts of the carapace have thus a more interwoven organization (Verma and Tomar, 2015: figs. 4, 5). Such a twisted organization can be observed in PB fossils (Fig. 9(D, E)). Taphonomic decay investigations showed the positive influence of chitin on soft tissue preservation in calcium phosphate for crustaceans, even preserving muscles, but the carapace decayed rapidly and was seldom preserved (Allison, 1988; Briggs and Kear, 1994). This suggests that the preservation of the carapace in PB shrimps involved early diagenetic processes. Therefore, differences in tissue composition between crustaceans and sponges could have played a role. More tests are needed in order to establish the origin of mineralisation differences between sponges and shrimps, and such inter-group comparisons are essential for discriminating taphonomic pathways. Modern imaging techniques as synchrotron-based XRF mapping have shown to be an efficient tool for obtaining critical morphological and chemical information (Bergmann et al., 2012; Anné et al., 2014; Gueriau and Bertrand, 2015; Gueriau et al., 2018), even in the case of flat fossils (Gueriau et al., 2014) like those from the Paris Biota (Brayard et al., 2019a).

#### 4.2. Influences of the immediate surrounding environment in early stages of fossilization

Differences in the sedimentary matrix can also be related to differences in preservation. Although the mineral composition of the matrix is similar for all the studied samples, clays are found in relatively high concentration around sponge fossils, whereas carbonates dominate around brachiopods (Figs. 2(I), 7(I); Brayard et al., 2017). Recent taphonomic experiments with clays showed the influence of these minerals during decay (Naimark et al., 2016; Newman et al., 2016). These experiences suggested that clays delay the decay of organic remains, favouring their preservation (Newman et al. 2016). This better preservation is likely linked to the inhibition of heterotrophic microorganisms activities in clays (McMahon et al., 2016). The occurrence of aluminium-bearing illite and albite in the PC sediments might be an effective preservative agent because of its tanning properties (Naimark et al. 2016). Recent observations of thylacocephalan fossils from La Voulte-sur-Rhône (middle Jurassic, France) have shown that clays are also able to replicate and preserve by themselves organic tissues at a cellular level (Vannier et al., 2016).

The unusual barite occurrence in at least two specimens of sponges may also provide further information on the preservation processes. The occurrence of Ba-rich sulphates is poorly documented in other *Fossil-Lagerstätten* but has been previously reported in the Burgess Shale (Conway Morris, 1985) and La Voulte-sur-Rhône sediments (Wilby et al., 1996). However, the occurrence of these small deposits of barite were scattered. Although the association of similar mineral phases (e.g., celestite, an Sr-sulphate) with sponges was also detected at La Voulte-sur-Rhône (Charbonnier, 2009), the formation of a complete mould of barite on top of fossilized organic remnants is a novelty as far as we know. In accordance with Raiswell et al. (2002), sedimentary barite can be formed by three pathways: (i) hydrothermalism, (ii) diagenesis or secondary circulation, and (iii) biotic photosynthetic activity. The Paris Canyon outcrop does not show any evidence of hydrothermal influence (Brayard et al., 2017). The origin of other occurrences of barite associated with fossils has been interpreted as authigenic/diagenetic, resulting from a very specific microenvironment generated during decay (Zabini et al., 2012). According to this hypothesis, barite can precipitate at the sulphate-methane transition zone within the sediment (Henkel et al., 2012). This suggests that several sponge fossils may have been enclosed in a different

microenvironment or even different microecosystems. However, the presence of this precipitate filling fossil cracks supports a delayed precipitation of this barite sulphate, during a subsequent phase of diagenesis. Such replenishment of fissure could be linked to the incidence of deep interstitial water circulation enriched in Ba. Metals would then precipitate as a result of the interaction with the chemosynthetic microorganisms present in the sediment (Johnson et al., 2004). In addition, this barite precipitation can be favoured by the presence of phosphatic precursors (Graber and Chafetz, 1990; Gonzalez-Muñoz et al., 2012), which can be formed during decay of carcasses (Briggs and Kear, 1993). However, the occurrence of Ba-rich sulphate in an anoxic and sulphate-reducing context could not be supported by the presence of pyrite framboids, which do not occur within the studied fossils. Consequently, more evidence is needed in order to better understand the influence of decay on barite formation.

#### *4.3. Potential preservation of organic material in shrimp shells*

Finally, the mineral characterization with Raman spectroscopy revealed the presence of unexpected peaks in the region of 1100-1500  $\text{cm}^{-1}$ , which can be linked to the preservation of organic elements. For instance, the  $\sim 1360 \text{ cm}^{-1}$  (1355) band detected in crustaceans can correspond with the D1-band of the graphite lattice (Wang et al., 1990). In addition, peaks at 1140, 1166, 1226, 1271, 1355,  $\sim 1470$  and  $1623 \text{ cm}^{-1}$  can correspond (with a slight shift) with  $\alpha$ -chitin reference frequently used as a standard (Wysokowski et al., 2014, 2015). Peaks between 1200 and  $1312 \text{ cm}^{-1}$  can be identified as the amide III bands (N-H) (Talari et al., 2015). The near absence of the expected G and D2 band peaks at  $\sim 1580 \text{ cm}^{-1}$  and  $\sim 1620 \text{ cm}^{-1}$ , respectively (or the presence of a small peak beneath the background), could be explained by the amorphous nature of the organic material preserved in the fossils (Kouketsu et al., 2014). However, this spectrum is different from the chitin spectrum detected in other fossil demosponges (Ehrlich et al., 2013), but these differences could also be related to the process of maturation and/or to the degree of preservation. Nevertheless, the exact origin of these peaks remains elusive.

## **5. Conclusion**

To sum-up, spectral analyses reveal a taxon-dependent preservation in the Paris Biota. The origin of these differences remains uncertain, but several potential factors can

be identified. Differences in the chemical composition of original tissues can explain variations in ultrastructure and quality of preservation. However, preservation can also be controlled by external factors such as the presence of clays and/or the occurrence of mineral deposits such as barite. These minerals can be potentially relevant for improving the exceptional preservation of organic remains such as the PB sponges. Therefore, the preservation potential of carcasses is determined by the combination of biological factors (e.g., the organic composition of tissues) and mineralization processes. In addition, the exceptional nature of the PB fossils can result from two interrelated processes. First, the Paris Biota could be an isolated, functionally atypical ecosystem whose unexpected diversity would not contradict the assumption that Early Triassic marine ecosystems were generally depauperate. Alternatively, this remarkable marine fauna could also be more widespread than previously thought; additional field investigations of sediments of this age will help to further testify this hypothesis. At present, there is no evidence for the occurrence of specific conditions that favoured the development of the Paris Biota. Thus, this remarkable marine benthic fauna may not be an exception during the Early Triassic. The mineralogical characterization and analyses of fossils herein exposed, combined with data resulting from taphonomic experiments, are essential for a consistent paleoecological reconstruction.

### **Acknowledgements**

We thank Olivier Beyssac (IMPMC, Paris) and Christine Stern (ICMUB, Dijon) for all the technical support and help with Raman and FTIR spectroscopies, respectively. This work is a contribution to the ANR project AFTER (ANR-13-JS06-0001-01) and was also supported by the French “Investissements d’Avenir” program, project ISITE-BFC (ANR-15-IDEX-03). We acknowledge the Bear Lake County road department and private land owner D. M. Clow (Ogden, Utah) for allowing access to the studied exposures.

### **References**

- Allison, P.A., 1988. The role of anoxia in the decay and mineralization of proteinaceous macro-fossils. *Paleobiology* 14, 139–154.
- Anné, J., Edwards, N.P., Wogelius, R.A., Tumarkin-Deratzian, A.R., Sellers, W.I., van Veelen, A., Bergmann, U., Sokaras, D., Alonso-Mori, R., Ignatyev, K., Egerton, V.M., Manning, P.L., 2014. Synchrotron imaging reveals bone healing and remodelling

- strategies in extinct and extant vertebrates. *Journal of the Royal Society Interface* 11, 2014.0277.
- Balthasar, U., 2007. An Early Cambrian organophosphatic brachiopod with calcitic granules. *Palaeontology* 50, 1319–1325.
- Beatty, T.W., Zonneveld, J.-P., Henderson, C.M., 2008. Anomalously diverse Early Triassic ichnofossil assemblages in northwest Pangea: A case for a shallow-marine habitable zone. *Geology* 36, 771.
- Bergmann, U., Manning, P.L., Wogelius, R.A., 2012. Chemical mapping of paleontological and archeological artifacts with synchrotron X-rays. *Annual Review of Analytical Chemistry*. 5, 361–89.
- Bernard, S., Benzerara, K., Beyssac, O., Balan, E., Brown Jr, G.E., 2015. Evolution of the macromolecular structure of sporopollenin during thermal degradation as documented by infrared, Raman and C-XANES spectroscopies. *Heliyon* 1, e00034.
- Bernard, S., Beyssac, O., Benzerara, K., 2008. Raman mapping using advanced line-scanning systems: geological applications. *Applied Spectroscopy*. 62, 1180–1188.
- Bernard, S., Beyssac, O., Benzerara, K., Findling, N., Tzvetkov, G., Brown, G.E., 2010. XANES, Raman and XRD study of anthracene-based cokes and saccharose-based chars submitted to high-temperature pyrolysis. *Carbon* 48, 2506–2516.
- Beyssac, O., Goffé, B., Petitet, J.-P., Froigneux, E., Moreau, M., Rouzaud, J.-N., 2003. On the characterization of disordered and heterogeneous carbonaceous materials by Raman spectroscopy. *Spectrochimica Acta Part A: Molecular and Biomolecular Spectroscopy* 59, 2267–2276.
- Botting, J.P., 2016. Diversity and ecology of sponges in the Early Ordovician Fezouata Biota, Morocco. *Palaeogeography, Palaeoclimatology, Palaeoecology* 460, 75–86.
- Botting, J.P., Brayard, A., the Paris Biota Team, 2019. A late-surviving Triassic protomonaxonid sponge from the Paris Biota (Bear Lake County, Idaho, USA). *Geobios* 52, xxx-xxx.
- Botting, J.P., Muir, L.A., Lin, J.P., 2013. Relationships of the Cambrian protomonaxonida (Porifera). *Palaeontologia Electronica* 460, 75–86.
- Bouligand, Y., 1965. Sur une architecture torsadée répandue dans de nombreuses cuticules d'arthropodes. *Comptes Rendus Hebdomadaire de l'Académie des Sciences* 261, 3665–3668.
- Brayard, A., Escarguel, G., Bucher, H., Monnet, C., Bruhwiler, T., Goudemand, N., Galfetti,

- T., Guex, J., 2009. Good genes and good luck: Ammonoid diversity and the end-Permian mass extinction. *Science* 325, 1118–1121.
- Brayard, A., Gueriau, P., Thoury, M., Escarguel, G., the Paris Biota Team, 2019a. Glow in the dark: use of synchrotron  $\mu$ XRF trace elemental mapping and multispectral macro-imaging on fossils from the Paris Biota (Bear Lake County, Idaho, USA). *Geobios* 52, xxx-xxx.
- Brayard, A., Jenks, J.F., Bylund, K.G., the Paris Biota Team, 2019b. Ammonoids and nautiloids from the earliest Spathian Paris Biota and other early Spathian localities in southeastern Idaho, USA. *Geobios* 52, xxx-xxx.
- Brayard, A., Krumenacker, L.J., Botting, J.P., Jenks, J.F., Bylund, K.G., Fara, E., Vennin, E., Olivier, N., Goudemand, N., Saucède, T., Charbonnier, S., Romano, C., Doguzhaeva, L., Thuy, B., Hautmann, M., Stephen, D.A., Thomazo, C., Escarguel, G., 2017. Unexpected Early Triassic marine ecosystem and the rise of the Modern evolutionary fauna. *Science Advance* 3, e1602159.
- Brayard, A., Meier, M., Escarguel, G., Fara, E., Nützel, A., Olivier, N., Bylund, K.G., Jenks, J.F., Stephen, D.A., Hautmann, M., Vennin, E., Bucher, H., 2015. Early Triassic Gulliver gastropods: Spatio-temporal distribution and significance for biotic recovery after the end-Permian mass extinction. *Earth-Science Reviews* 146, 31–64.
- Briggs, D.E.G., Kear, A.J., 1994. Decay and mineralization of shrimps. *Palaios* 9, 431–456.
- Briggs, D.E.G., Kear, A.J., 1993. Fossilization of soft tissue in the laboratory. *Science* 259, 1439–1442.
- Brunner, E., Ehrlich, H., Schupp, P., Hedrich, R., Hunoldt, S., Kammer, M., Machill, S., Paasch, S., Bazhenov, V.V., Kurek, D.V., Arnold, T., Brockmann, S., Ruhnow, M., Born, R., 2009. Chitin-based scaffolds are an integral part of the skeleton of the marine demosponge *Ianthella basta*. *Journal of Structural Biology* 168, 539–547.
- Butler, A.D., Cunningham, J.A., Budd, G.E., Donoghue, P.C.J., 2015. Experimental taphonomy of *Artemia* reveals the role of endogenous microbes in mediating decay and fossilization. *Proceedings of the Royal Society, Biological Sciences* 282, 2015.0476.
- Charbonnier, S., 2009. Le Lagerstätte de La Voulte : un environnement bathyal au Jurassique. Publications scientifiques du Muséum.
- Charbonnier, S., Brayard, A., the Paris Biota Team, 2019. New thylacocephalans from the Early Triassic Paris Biota (Bear Lake County, Idaho, USA). *Geobios* 52, xxx-xxx.

- Clements, T., Colleary, C., De Baets, K., Vinther, J., 2017. Buoyancy mechanisms limit preservation of coleoid cephalopod soft tissues in Mesozoic Lagerstätten. *Palaeontology* 60, 1–14.
- Conway Morris, S., 1985. Concluding Remarks: Extraordinary fossil biotas: Their ecological and evolutionary significance. *Royal Society of London Philosophical Transactions B* 311, 187–192.
- Doguzhaeva, L.A., Brayard, A., Goudemand, N., Krümenacker, L.J., Jenks, J.F., Bylund, K.G., Fara, E., Olivier, N., Vennin, E., Escarguel, G., 2018. An Early Triassic gladius associated with soft tissue remains from Idaho, USA—a squid-like coleoid cephalopod at the onset of Mesozoic Era. *Acta Palaeontologica Polonica* 63, 341–355.
- Ehrlich, H., Ilan, M., Maldonado, M., Muricy, G., Bavestrello, G., Kljajic, Z., Carballo, J.L., Schiaparelli, S., Ereskovsky, A., Schupp, P., Born, R., Worch, H., Bazhenov, V.V., Kurek, D., Varlamov, V., Vyalikh, D., Kummer, K., Sivkov, V.V., Molodtsov, S.L., Meissner, H., Richter, G., Steck, E., Richter, W., Hunoldt, S., Kammer, M., Paasch, S., Krasokhin, V., Patzke, G., Brunner, E., 2010. Three-dimensional chitin-based scaffolds from *Verongida* sponges (Demospongiae: Porifera). Part I. Isolation and identification of chitin. *International Journal of Biological Macromolecules* 47, 132–140.
- Ehrlich, H., Rigby, J.K., Botting, J.P., Tsurkan, M. V., Werner, C., Schwille, P., Petrášek, Z., Pisera, A., Simon, P., Sivkov, V.N., Vyalikh, D. V., Molodtsov, S.L., Kurek, D., Kammer, M., Hunoldt, S., Born, R., Stawski, D., Steinhof, A., Bazhenov, V. V., Geisler, T., 2013. Discovery of 505-million-year old chitin in the basal demosponge *Vauxia gracilenta*. *Scientific Reports* 3, 3497.
- Foster, W.J., Danise, S., Sedlacek, A., Price, G.D., Hips, K., Twitchett, R.J., 2015. Environmental controls on the post-Permian recovery of benthic, tropical marine ecosystems in western Palaeotethys (Aggtelek Karst, Hungary). *Palaeogeography, Palaeoclimatology, Palaeoecology* 440, 374–394.
- Galfetti, T., Bucher, H., Ovtcharova, M., Schaltegger, U., Brayard, A., Brühwiler, T., Goudemand, N., Weissert, H., Hochuli, P.A., Cordey, F., Guodun, K., 2007. Timing of the Early Triassic carbon cycle perturbations inferred from new U–Pb ages and ammonoid biochronozones. *Earth and Planetary Science Letters* 258, 593–604.
- Gonzalez-Muñoz, M.T., Martinez-Ruiz, F., Morcillo, F., Martin-Ramos, J.D., Paytan, A.,

2012. Precipitation of barite by marine bacteria: A possible mechanism for marine barite formation. *Geology* 40, 675–678.
- Graber, K.K., Chafetz, H.S., 1990. Petrography and origin of bedded barite and phosphate in the Devonian Slaven Chert of central Nevada. *Journal of Sedimentary Research* 60, 897–911.
- Grasby, S.E., Beauchamp, B., Embry, A., Sanei, H., 2013. Recurrent Early Triassic ocean anoxia. *Geology* 41, 175–178.
- Griesshaber, E., Kelm, K., Sehrbrock, A., Mader, W., Mutterlose, J., Brand, U., Schmahl, W.W., 2009. Amorphous calcium carbonate in the shell material of the brachiopod *Megerlia truncata*. *European Journal of Mineralogy* 21, 715–723.
- Gueriau, P., Bertrand, L., 2015. Deciphering exceptional preservation of fossils through trace elemental imaging. *Microscopy Today* 23, 20–25.
- Gueriau, P., Jauvion, C., Mocuta, C., 2018. Show me your yttrium, and I will tell you who you are: implications for fossil imaging. *Palaeontology* 61, 981–990.
- Gueriau, P., Mocuta, C., Dutheil, D.B., Cohen, S.X., Thiaudière, D., Charbonnier, S., Clément, G., Bertrand, L., 2014. Trace elemental imaging of rare earth elements discriminates tissues at microscale in flat fossils. *Plos One* 9, e86946.
- Gupta, N.S., 2011. Chitin: formation and diagenesis. Springer Netherlands, Houten.
- Gupta, N.S., Michels, R., Briggs, D.E.G., Collinson, M.E., Evershed, R.P., Pancost, R.D., 2007. Experimental evidence for the formation of geomacromolecules from plant leaf lipids. *Organic Geochemistry* 38, 28–36.
- Gupta, N.S., Michels, R., Briggs, D.E.G., Evershed, R.P., Pancost, R.D., 2006. The organic preservation of fossil arthropods: an experimental study. *Proceedings of the Royal Society of London, Biological Sciences* 273, 2777–2783.
- Henkel, S., Mogollón, J.M., Nöthen, K., Franke, C., Bogus, K., Robin, E., Bahr, A., Blumenberg, M., Pape, T., Seifert, R., März, C., de Lange, G.J., Kasten, S., 2012. Diagenetic barium cycling in Black Sea sediments – A case study for anoxic marine environments. *Geochimica et Cosmochimica Acta* 88, 88–105.
- Hof, C.H.J., Briggs, D.E.G., 1997. Decay and mineralization of mantis shrimps (Stomatopoda: Crustacea): a key to their fossil record. *Palaios* 12, 420–438.
- Hofmann, R., Hautmann, M., Brayard, A., Nützel, A., Bylund, K.G., Jenks, J.F., Vennin, E., Olivier, N., Bucher, H., 2014. Recovery of benthic marine communities from the end-Permian mass extinction at the low latitudes of eastern Panthalassa.

- Palaeontology 57, 547–589.
- Iniesto, M., Laguna, C., Florín, M., Guerrero, M.C., Chicote, Á., Buscalioni, Á.D., López-Archilla, A.I., 2015. The impact of microbial mats and their microenvironmental conditions in early decay of fish. *Palaios* 30, 792–801.
- Iniesto, M., López-Archilla, A.I., Fregenal-Martínez, M.A., Buscalioni, Á.D., Guerrero, M.C., 2013. Involvement of microbial mats in delayed decay: An experimental essay on fish preservation. *Palaios* 28, 56–66.
- Iniesto, M., Villalba, I., Buscalioni, A.D., Guerrero, M.C., López-Archilla, A.I., 2017. The effect of microbial mats in the decay of anurans with implications for understanding taphonomic processes in the fossil record. *Scientific Reports* 7, 45160.
- Jattiot, R., Bucher, H., Brayard, A., Monnet, C., Jenks, J.F., Hautmann, M., 2016. Revision of the genus *Anasibirites* Mojsisovics (Ammonoidea): an iconic and cosmopolitan taxon of the late Smithian (Early Triassic) extinction. *Papers in Palaeontology* 2, 155–188.
- Johnson, C.A., Kelley, K.D., Leach, D.L., 2004. Sulfur and Oxygen isotopes in barite deposits of the western Brooks Range, Alaska, and implications for the origin of the Red Dog massive sulfide deposits. *Economic Geology* 99, 1435–1448.
- Kouketsu, Y., Mizukami, T., Mori, H., Endo, S., Aoya, M., Hara, H., Nakamura, D., Wallis, S., 2014. A new approach to develop the Raman carbonaceous material geothermometer for low-grade metamorphism using peak width. *Island Arc* 23, 33–50.
- Mahamid, J., Aichmayer, B., Shimoni, E., Ziblat, R., Li, C., Siegel, S., Paris, O., Fratzl, P., Weiner, S., Addadi, L., 2010. Mapping amorphous calcium phosphate transformation into crystalline mineral from the cell to the bone in zebrafish fin rays. *Proceedings of the National Academy of Sciences of the United States of America* 107, 6316–6321.
- Mahamid, J., Sharir, A., Addadi, L., Weiner, S., 2008. Amorphous calcium phosphate is a major component of the forming fin bones of zebrafish: Indications for an amorphous precursor phase. *Proceedings of the National Academy of Sciences of the United States of America* 105, 12748–12753.
- Martin, D., Briggs, D.E.G., Parkes, R.J., 2005. Decay and mineralization of invertebrate eggs. *Palaios* 20, 562–572.

- McMahon, S., Anderson, R.P., Saupe, E.E., Briggs, D.E.G., 2016. Experimental evidence that clay inhibits bacterial decomposers: Implications for preservation of organic fossils. *Geology* 44, 867–870.
- Muir, L.A., Botting, J.P., Carrera, M.G., Beresi, M., 2013. Cambrian, Ordovician and Silurian non-stromatoporoid Porifera. Geological Society of London, Special Publication 38, 81–95.
- Naimark, E., Kalinina, M., Shokurov, A., Boeva, N., Markov, A., Zaytseva, L., 2016. Decaying in different clays: implications for soft-tissue preservation. *Palaeontology* 59, 583–595.
- Newman, S.A., Mariotti, G., Pruss, S., Bosak, T., 2016. Insights into cyanobacterial fossilization in Ediacaran siliciclastic environments. *Geology* 44, 579–582.
- Orchard, M.J., 2007. Conodont diversity and evolution through the latest Permian and Early Triassic upheavals. *Palaeogeography, Palaeoclimatology, Palaeoecology* 252, 93–117.
- Payne, J.L., Clapham, M.E., 2012. End-Permian mass extinction in the oceans: an ancient analog for the Twenty-First Century? *Annual Review of Earth and Planetary Sciences* 40, 89–111.
- Payne, J.L., Lehrmann, D.J., Wei, J., Orchard, M.J., Schrag, D.P., Knoll, A.H., 2004. Large perturbations of the carbon cycle during recovery from the end-Permian extinction. *Science* 305, 506–509.
- Raff, E.C., Andrews, M.E., Turner, F.R., Toh, E., Nelson, D.E., Raff, R.A., 2013. Contingent interactions among biofilm-forming bacteria determine preservation or decay in the first steps toward fossilization of marine embryos. *Evolution and Development* 15, 243–256.
- Raff, E.C., Schollaert, K.L., Nelson, D.E., Donoghue, P.C.J., Thomas, C.-W., Turner, F.R., Stein, B.D., Dong, X., Bengtson, S., Hultgren, T., Stampanoni, M., Chongyu, Y., Raff, R.A., 2008. Embryo fossilization is a biological process mediated by microbial biofilms. *Proceedings of the National Academy of Sciences of the United States of America* 105, 19360–19365.
- Raff, E.C., Villinski, J., Turner, F.R., Donoghue, P.C.J., Raff, R.A., 2006. Experimental taphonomy shows the feasibility of fossil embryos. *Proceedings of the National Academy of Sciences of the United States of America* 103, 5846–5851.
- Raiswell, R., Bottrell, S.H., Dean, S.P., Marshall, J.D., Carr, A., Hatfield, D., 2002. Isotopic

- constraints on growth conditions of multiphase calcite-pyrite-barite concretions in Carboniferous mudstones. *Sedimentology* 49, 237–254.
- Raup, D.M., 1979. Size of the Permo-Triassic bottleneck and its evolutionary implications. *Science* 206, 217–218.
- Rigby, J.K., Collins, D., 2004. Sponges of the Middle Cambrian Burgess Shale and Stephen Formations, British Columbia. Royal Ontario Museum.
- Romano, C., Argyriou, T., Krumenacker L.J., the Paris Biota Team, 2019. Chondrichthyan teeth from the Early Triassic Paris Biota (Bear Lake County, Idaho, USA). *Geobios* 52, xxx-xxx.
- Romano, C., Goudemand, N., Vennemann, T.W., Ware, D., Schneebeli-Hermann, E., Hochuli, P.A., Brühwiler, T., Brinkmann, W., Bucher, H., 2013. Climatic and biotic upheavals following the end-Permian mass extinction. *Nature Geoscience* 6, 57–60.
- Sagemann, J., Bale, S.J., Briggs, D.E.G., Parkes, R.J., 1999. Controls on the formation of authigenic minerals in association with decaying organic matter: An experimental approach. *Geochimica et Cosmochimica Acta* 63, 1083–1095.
- Sansom, R.S., 2016. Preservation and phylogeny of Cambrian ecdysozoans tested by experimental decay of *Priapulid*. *Scientific Reports* 6, 32817.
- Sansom, R.S., Gabbott, S.E., Purnell, M.A., 2010. Decay of vertebrate characters in hagfish and lamprey (Cyclostomata) and the implications for the vertebrate fossil record. *Proceedings of the Royal Society of London, Biological Sciences* 278, 1150–1157.
- Saucède, T., Vennin, E., Fara, E., Olivier, N., the Paris Biota Team, 2019. A new holocrinid (Articulata) from the Paris Biota (Bear Lake County, Idaho, USA) highlights the high diversity of Early Triassic crinoids. *Geobios* 52, xxx-xxx.
- Seilacher, A., 1970. Begriff und bedeutung der Fossil-Lagerstätten. *Neues Jahrbuch für Geologie und Paläontologie, Monatshefte* 1, 34–39.
- Seilacher, A., Reif, W.-E., Westphal, F., Riding, R., Clarkson, E.N.K., Whittington, H.B., 1985. Sedimentological, Ecological and Temporal Patterns of Fossil Lagerstätten. *Philosophical Transactions of the Royal Society of London* 311, 5–24.
- Sun, Y., Joachimski, M.M., Wignall, P.B., Yan, C., Chen, Y., Jiang, H., Wang, L., Lai, X., 2012. Lethally hot temperatures during the Early Triassic greenhouse. *Science* 338, 366–370.
- Talari, A.C.S., Movasaghi, Z., Rehman, S., Rehman, I.U., 2015. Raman spectroscopy of biological tissues. *Applied Spectroscopy Reviews* 50, 46–111.

- Thomazo, C., Brayard, A., Elmeknassi, S., Vennin, E., Olivier, N., Caravaca, G., Escarguel, G., Fara, E., Bylund, K.G., Jenks, J.F., Stephen, D.A., Killingsworth, B., Sansjofre, P., Cartigny, P. in press. Multiple sulfur isotope signals associated with the late Smithian event and the Smithian/Spathian boundary. *Earth-Science Reviews*. DOI: 10.1016/j.earscirev.2018.06.019.
- Thomazo, C., Vennin, E., Brayard, A., Bour, I., Mathieu, O., Elmeknassi, S., Olivier, N., Escarguel, G., Bylund, K.G., Jenks, J., Stephen, D.A., Fara, E., 2016. A diagenetic control on the Early Triassic Smithian-Spathian carbon isotopic excursions recorded in the marine settings of the Thaynes Group (Utah, USA). *Geobiology* 14, 220–236.
- Thuy, B., Escarguel, G., the Paris Biota Team, 2019. A new brittle star (Ophiuroidea: Ophiodermatina) from the Early Triassic Paris Biota (Bear Lake County, Idaho, USA). *Geobios* 52, xxx-xxx.
- Vannier, J., Schoenemann, B., Gillot, T., Charbonnier, S., Clarkson, E., 2016. Exceptional preservation of eye structure in arthropod visual predators from the Middle Jurassic. *Nature Communications* 7, 10320.
- Verma, D., Tomar, V., 2015. An investigation into mechanical strength of exoskeleton of hydrothermal vent shrimp (*Rimicaris exoculata*) and shallow water shrimp (*Pandalus platyceros*) at elevated temperatures. *Materials Science and Engineering C* 49, 243–250.
- Wang, Q., Morse, J.W., 1996. Pyrite formation under conditions approximating those in anoxic sediments I. Pathway and morphology. *Marine Chemistry* 52, 99–121.
- Wang, Y., Alsmeyer, D.C., McCreery, R.L., 1990. Raman spectroscopy of carbon materials: structural basis of observed spectra. *Chemistry of Materials* 2, 557–563.
- Wilby, P.R., Briggs, D.E.G., Riou, B., 1996. Mineralization of soft-bodied invertebrates in a Jurassic metalliferous deposit. *Geology* 24, 847-850.
- Williams, A., Cusack, M., Buckman, J.O., 1998. Chemico-structural phylogeny of the discinoid brachiopod shell. *Philosophical Transactions of The Royal Society B* 353, 2005–2038.
- Wilson, P., Parry, L.A., Vinther, J., Edgecombe, G.D., 2016. Unveiling biases in soft-tissue phosphatization: extensive preservation of musculature in the Cretaceous (Cenomanian) polychaete *Rollinschaeta myoplana* (Annelida: Amphinomidae). *Palaeontology* 59, 463–479.

- Wysokowski, M., Motylenko, M., Walter, J., Lota, G., Wojciechowski, J., Stöcker, H., Galli, R., Stelling, A.L., Himcinski, C., Niederschlag, E., Langer, E., Bazhenov, V. V., Szatkowski, T., Zdart, J., Pertenko, I., Kljajić, Z., Leisegang, T., Molodtsov, S.L., Meyer, D.C., Jesionowski, T., Ehrlich, H., 2014. Synthesis of nanostructured chitin-hematite composites under extreme biomimetic conditions. *Royal Society of Chemistry Advances* 4, 61743–61752.
- Wysokowski, M., Petrenko, I., Motylenko, M., Langer, E., Bazhenov, V. V., Galli, R., Stelling, A.L., Kljajić, Z., Szatkowski, T., Kutsova, V.Z., Stawski, D., Jesionowski, T., 2015. Renewable chitin from marine sponge as a thermostable biological template for hydrothermal synthesis of hematite nanospheres using principles of extreme biomimetics. *Bioinspired Materials* 1, 12-22.
- Zabini, C., Schiffbauer, J.D., Xiao, S., Kowalewski, M., 2012. Biomineralization, taphonomy, and diagenesis of Paleozoic lingulide brachiopod shells preserved in silicified mudstone concretions. *Palaeogeography, Palaeoclimatology, Palaeoecology* 326–328, 118–127.
- Zimmermann, E.A., Gludovatz, B., Schaible, E., Dave, N.K.N., Yang, W., Meyers, M.A., Ritchie, R.O., 2013. Mechanical adaptability of the Bouligand-type structure in natural dermal armour. *Nature Communications* 4, 2634.

## Table and Figure captions

**Table 1.** List of the studied specimens and associated analyses (stars indicate specimens lost during the preparation process).

**Table 2.** Identification of bands in the Raman spectrum of discinoid fossils and HAP reference (Fig. 4(B)).

**Fig. 1.** Mineralogy of the Paris Biota sedimentary matrix. **A.** SEM image of the sedimentary matrix of the discinoid brachiopod specimen UBGD 30626. **B-F.** EDXS maps of Ca, Si, Al, K and Mg, respectively. **G.** EDXS spectrum of the zone depicted in A. **H.** XRD diffractogram of the sediment powder. Ch: chlorite; ill: illite; Qx: Quartz; Alb: Albite; Ca: Calcite. Scale bar: 500  $\mu\text{m}$  (A).

**Fig. 2.** SEM images of discinoid (A-I) and linguloid (J-M) brachiopods. **A.** General view of the discinoid specimen UBGD 30626. **B.** View of growth annuli preserved in discinoid fossil UBGD 30626. **C.** Close-up view showing rod-shaped crystals for specimen UBGD 30626. **D.** Concentric annuli of discinoid shells are sometimes preserved as an impression. **E.** Remain of the discinoid shell UBGD 30631. **F-H.** EDXS maps of E, showing the location of Si, Ca and P, respectively. **I.** Image mixing EDXS maps showed in F-H. The pink colour results from the overlapping of Ca and P signals. The absence of P in the zone highlighted by the arrow is noticeable, showing the replacement of the calcium phosphate by carbonates during diagenesis. **J.** General view of the linguloid specimen UBGD 30641. **K, L.** View of growth annuli (arrows). **M.** Close-up view showing pores in the mineralized shell. Scale bars: 500  $\mu\text{m}$  (A, J), 100  $\mu\text{m}$  (B, D, E, K, L), 5  $\mu\text{m}$  (C), 10  $\mu\text{m}$  (M).

**Fig. 3.** Mineralogical characterization of discinoids and linguloids. **A.** SEM picture of the edge of the shell of the discinoid brachiopod UBGD 30629 (white arrow) and its surrounding matrix (black arrow). **B-D.** EDXS maps of A, showing the location of Si, Ca and P, respectively. **E.** Image mixing EDXS maps showed in B-D. The pink colour results from the overlapping of Ca and P signals. **F.** SEM picture of the linguloid shell

UBGD 30640. **G-I**. EDXS maps of F, showing the location of Si, Ca and P, respectively. **J**. Image mixing EDXS maps showed in F-H. **K**. FTIR spectra of the linguloid and discinoid specimens UBGD 30627 and UBGD 30640, respectively. Reference spectra for calcite and hydroxyapatite are also illustrated. Bands relevant for identification have been highlighted by purple (HAP) and cyan (calcite) arrows. Scale bars: 100  $\mu\text{m}$  (A, F).

**Fig. 4.** EDXS and Raman spectra of discinoid fossils. **A**. EDXS map of UBGD 30631 showing the presence of Ca and P as major components of the mineralized structure. **B**. Identification of calcium phosphate using Raman. Brachiopod spectrum (UBGD 30633, in black) is compared to hydroxyapatite, fluorapatite and chlorapatite spectra. Peaks relevant for identification have been highlighted (Table 2).

**Fig. 5.** SEM observation of caridean shrimps and mineralogical characterization using FTIR. **A**. General view of the shrimp specimen UBGD 30638 under UV light. **B**. View of the mineralized remains over the sediment matrix (arrow). **C**. Close-up view of the fossil showing holes in mineral (arrows). **D**. At higher magnification, even mineralized zones in C show the occurrence of these pores (arrows). **E**. General SEM view of the shrimp specimen UBGD 30636 showing that several parts of the exoskeleton are missing. **F-H**. EDXS maps of E, showing the location of Si, Ca and P, respectively. **I**. Image mixing EDXS maps showed in F-H. The pink colour results from the overlapping of Ca and P signals. **J**. FTIR spectra of calcite, hydroxyapatite and of the caridean shrimp specimen UBGD 30638. Bands relevant for identification are indicated by purple (HAP) and cyan (calcite) arrows. Scale bars: 1 cm (A), 200  $\mu\text{m}$  (B), 2  $\mu\text{m}$  (C), 1  $\mu\text{m}$  (D), 500  $\mu\text{m}$  (E).

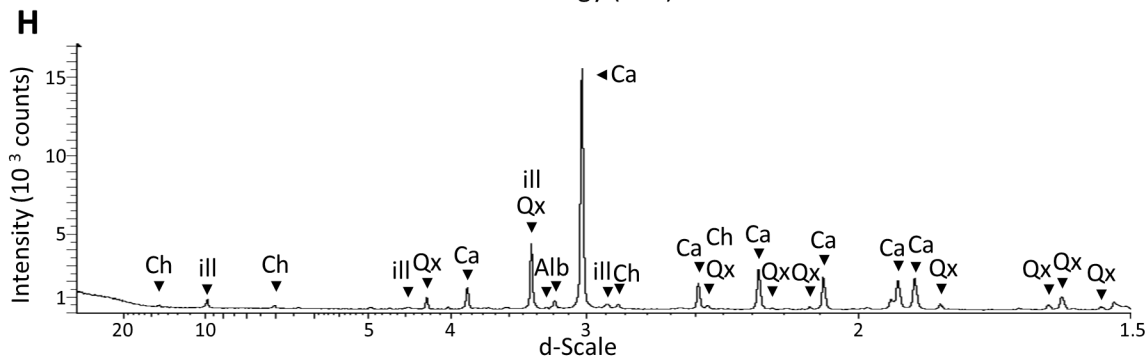
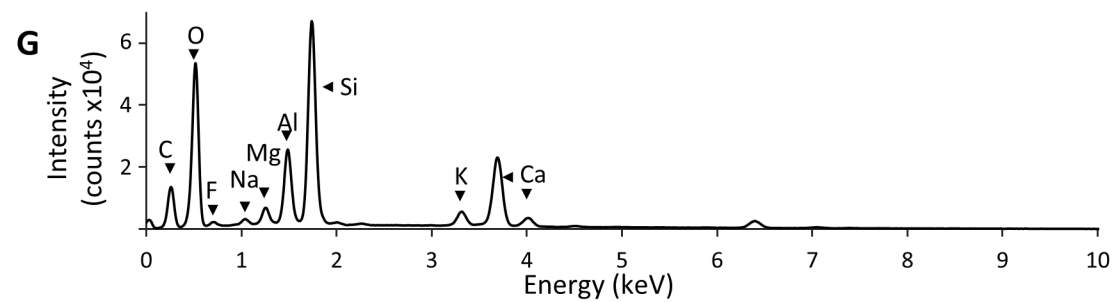
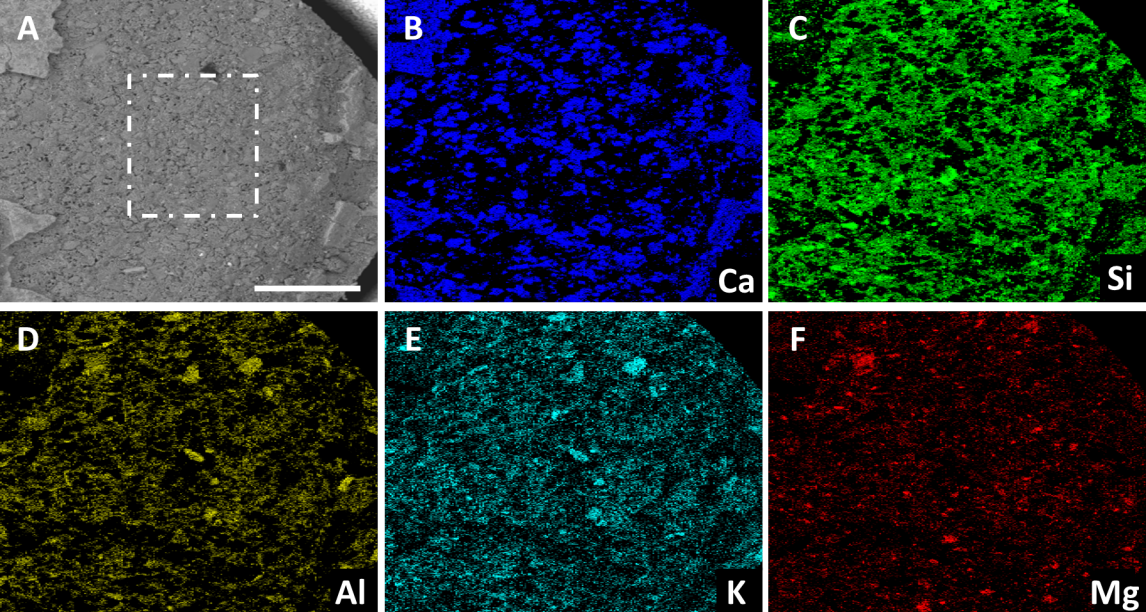
**Fig. 6.** Raman spectra (focused in the region 800-1800  $\text{cm}^{-1}$ ) of two caridean shrimp fossil specimens (UBGD 30635 and UBGD 30636). Peaks relevant for potential identification have been highlighted.

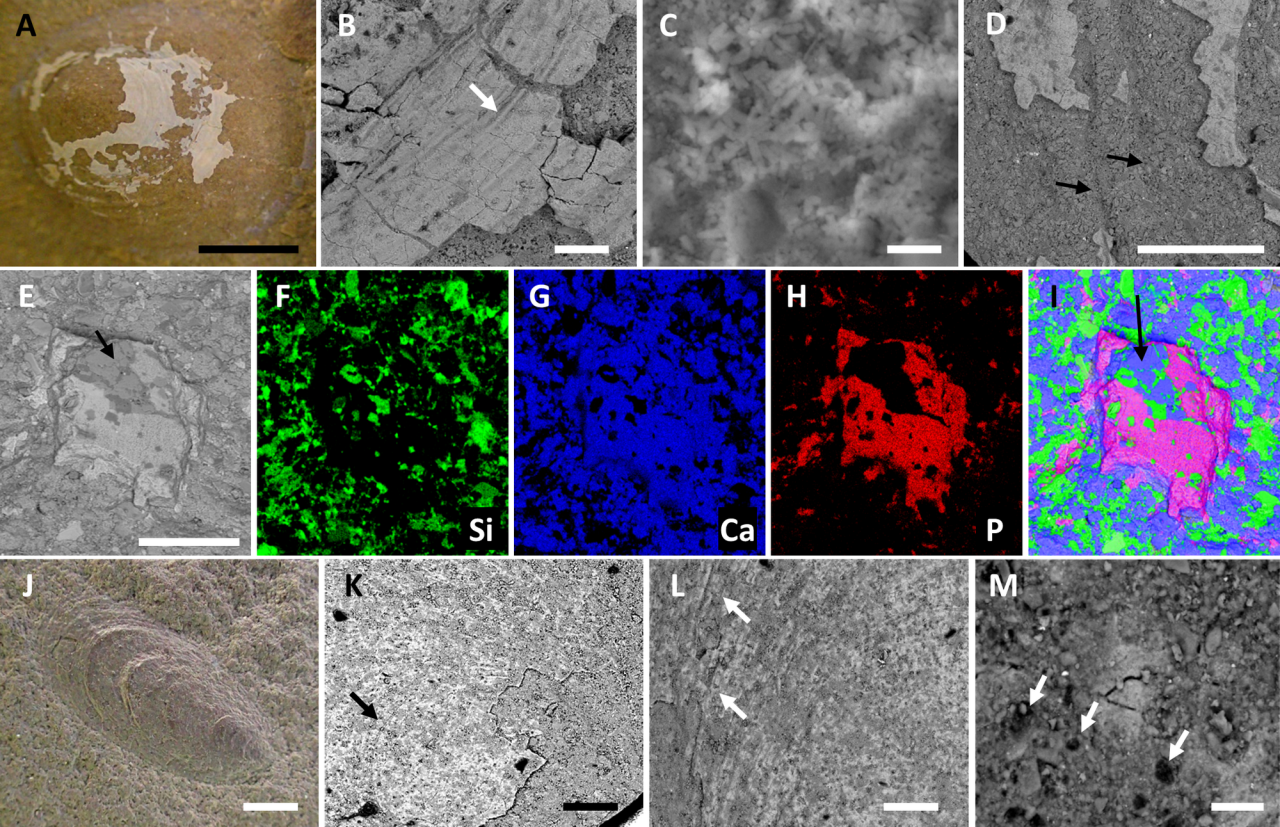
**Fig. 7.** SEM-EDXS and FTIR analyses of sponge fossils. **A**. Photograph of specimen UBGD 30617. **B**. Three-dimensional preservation of the external part of the sponge specimen UBGD 30619. The white arrow points to an inner layer, whereas the external face is indicated by black arrows. Dotted lines mark the edge between the two layers. **C**. Close-up view of the inner layer. **D**. At higher magnification, the inner layer shows a very

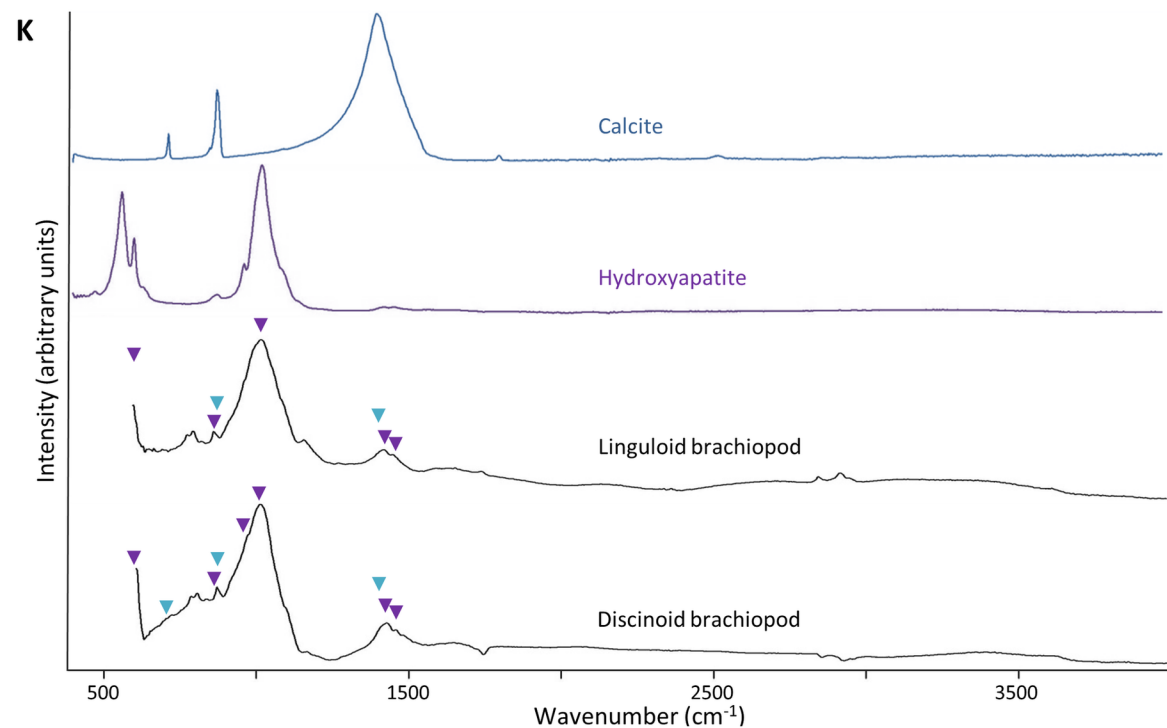
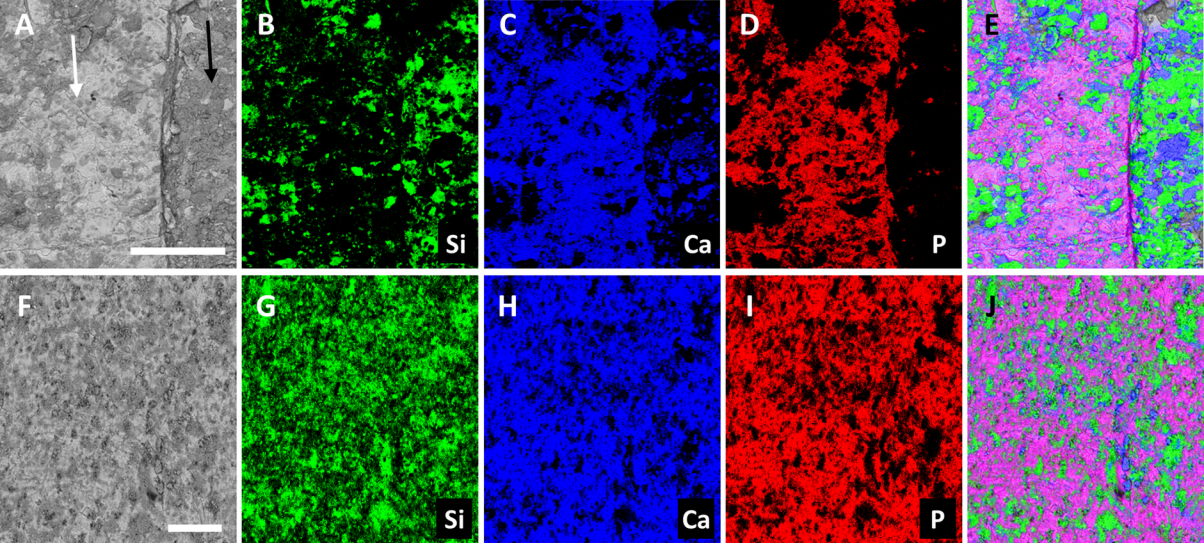
homogenous mineralogical structure. **E.** General SEM view of the sponge specimen UBGD 30617 over the sediment (arrow). **F-H.** EDXS maps of E, showing the location of Si, Ca and P, respectively. **I.** Image mixing EDXS maps showed in F-H. The pink colour results from the overlapping of Ca and P signals. **J.** FTIR spectra of calcite, hydroxyapatite and the sponge specimen UBGD 30613. Bands relevant for identification have been highlighted by purple (HAP) and cyan (calcite) arrows. Scale bars: 500  $\mu\text{m}$  (A), 100  $\mu\text{m}$  (B, E), 5  $\mu\text{m}$  (C), 1  $\mu\text{m}$  (D).

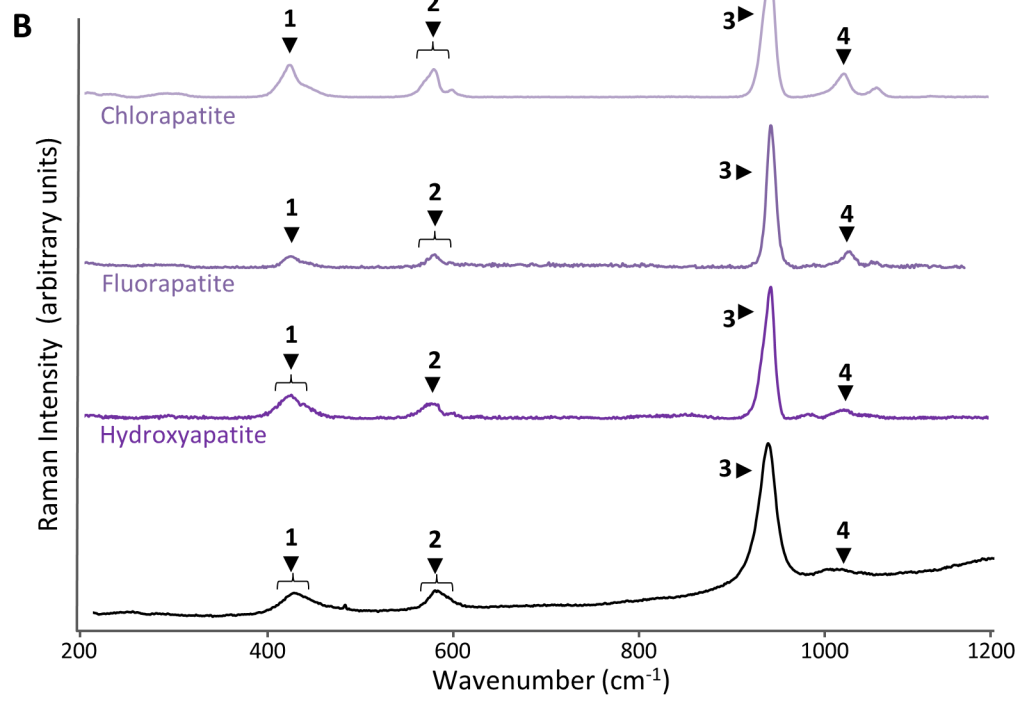
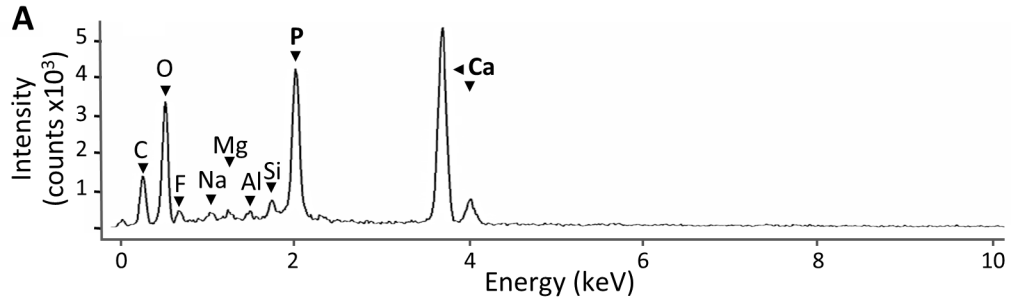
**Fig. 8.** SEM-EDXS images of the mineral cover detected in sponge specimen UBGD 30621. **A.** SEM image of the precipitate covering the fossil. In contrast with previous images, in which the fossil looks brighter than the sediment, here the fossil is darker than the covering mineral. **B-E.** EDXS maps of A, showing the location of Ba, S, Ca and P, respectively. **F.** View of the Ba-rich deposit over the fossil and also beneath it (arrow). **G.** Ba-rich precipitate filling cracks of the fossil. **H.** Close-up view of the crack. **I.** Raman spectra of calcite, barite and the sponge specimen UBGD 30623. In addition to calcite (purple), several characteristic bands of barite (green) are present. Scale bars: 100  $\mu\text{m}$  (A, F), 10  $\mu\text{m}$  (G), 1  $\mu\text{m}$  (H).

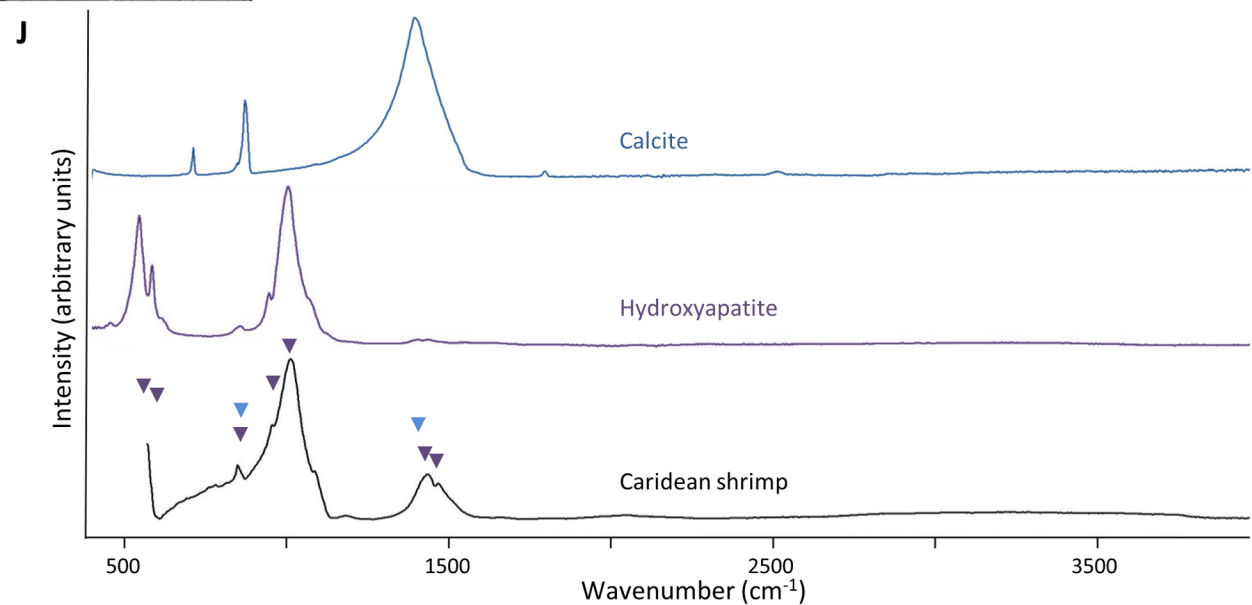
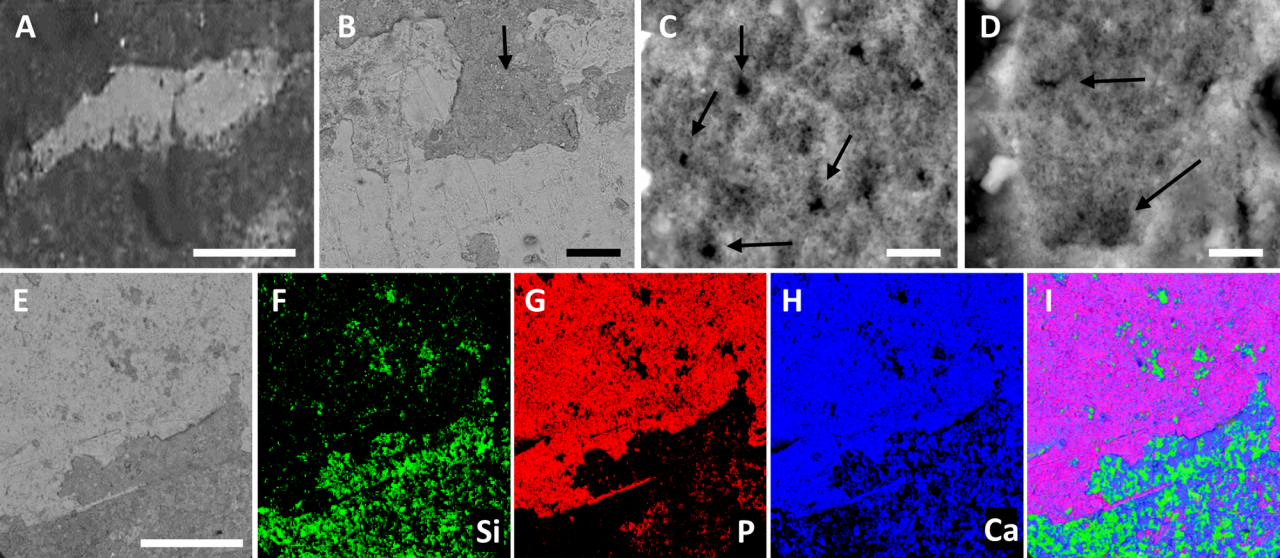
**Fig. 9.** SEM identification of a clade-related ultrastructure of calcium phosphate in discinoid brachiopods (**A**), caridean shrimps (**D**) and leptomitid sponges (**G**) from the PB. In discinoids, mineral crystals are larger (~400 nm length; **C**) than in sponges (~100 nm length; **I**) or shrimps (crystals composed of small amorphous round aggregates; **F**). In addition, they do not exhibit any preferential orientation, in contrast to leptomitid sponges. In shrimps, crystals show a complex and convoluted organization in fibres (dotted lines in D and E). Collection numbers: A, B: UBGD 30625; C: UBGD 30626; D-F: UBGD 30637; G, H: UBGD 30621; I: UBGD 30617. Scale bars: 1  $\mu\text{m}$  (A, D, G), 500 nm (B, E, H), 100 nm (C, F, I).

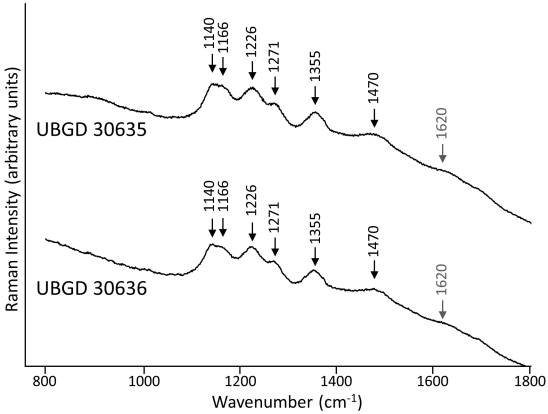


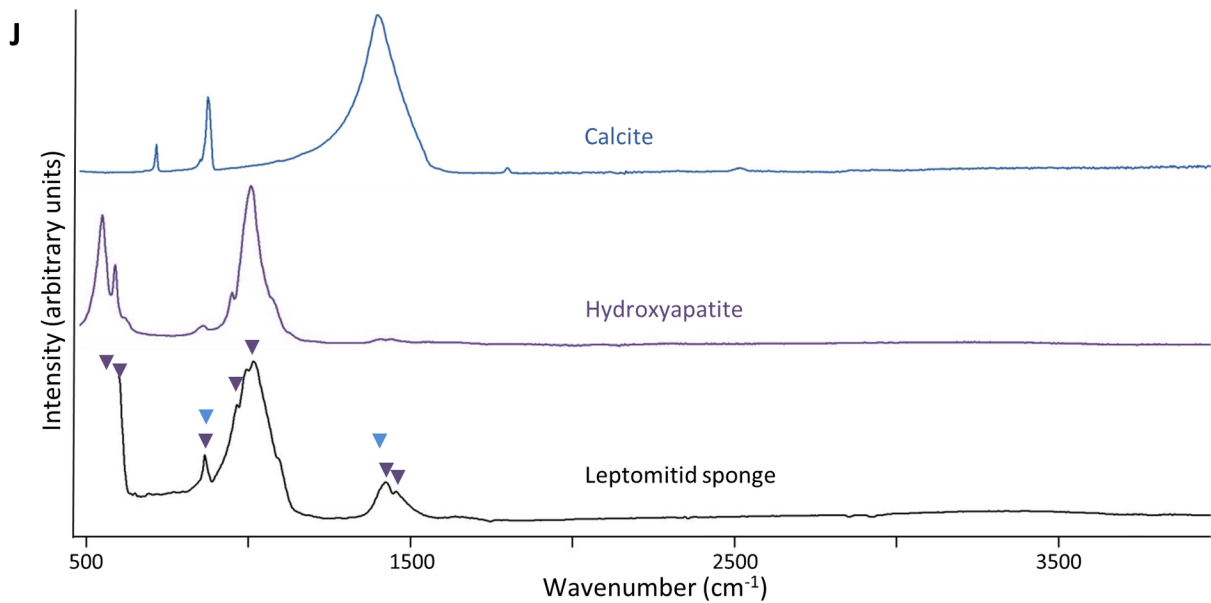
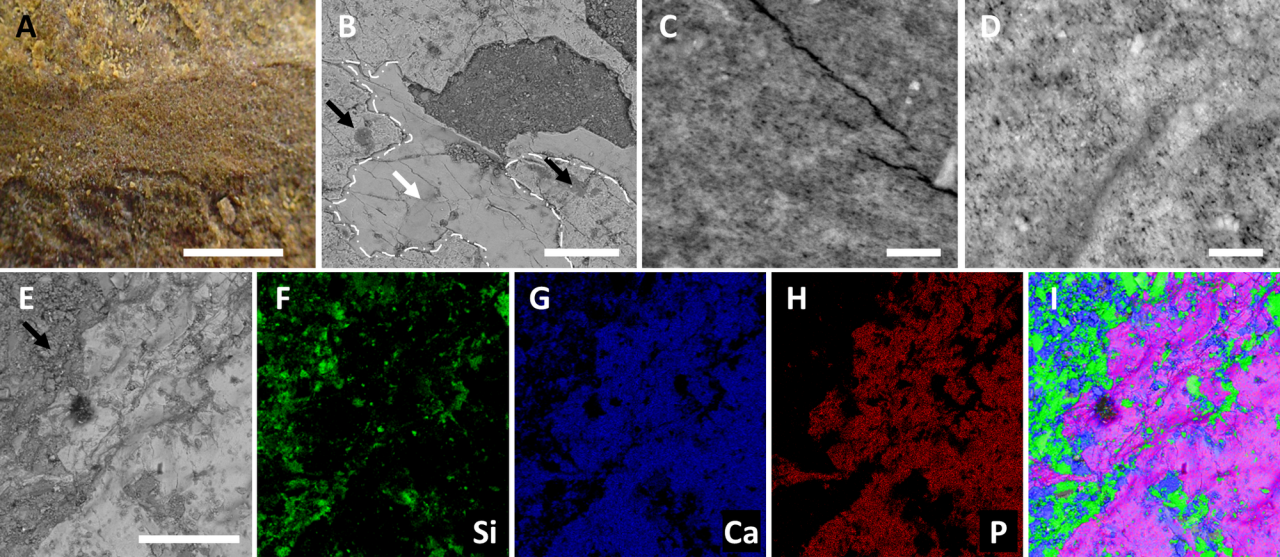


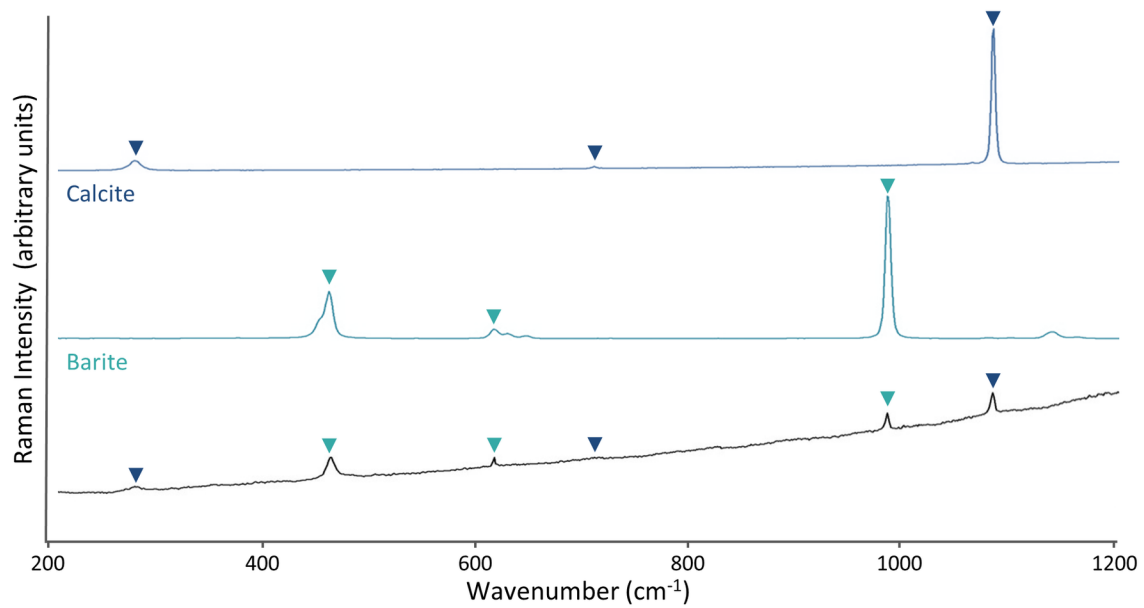
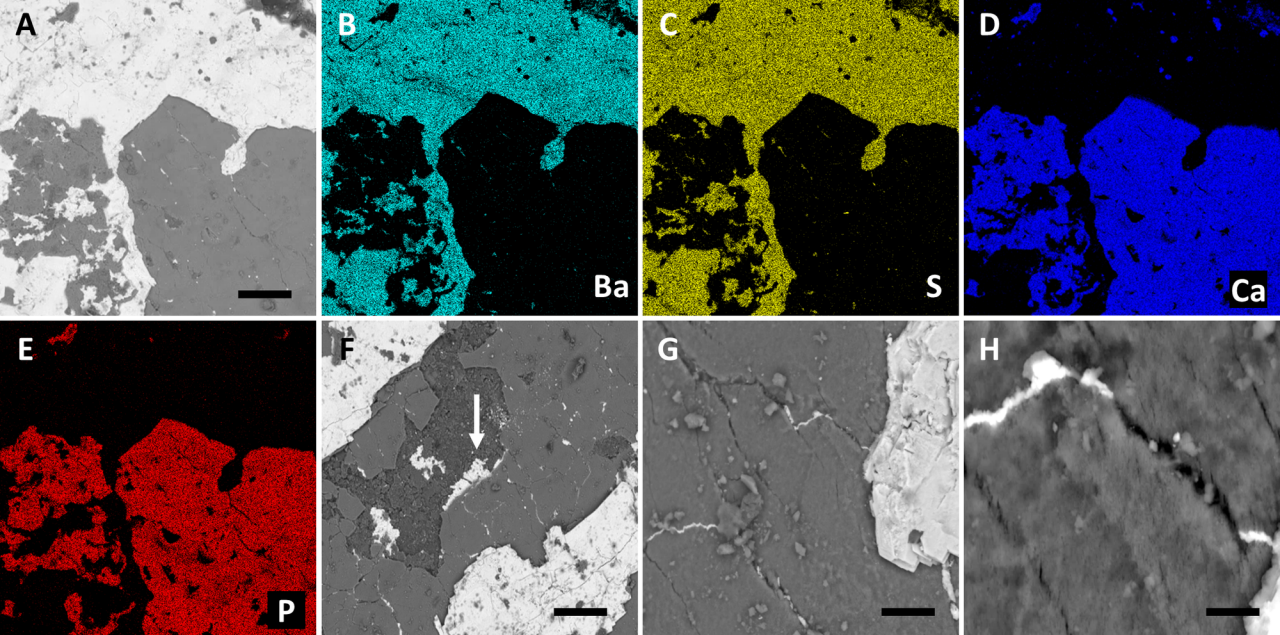












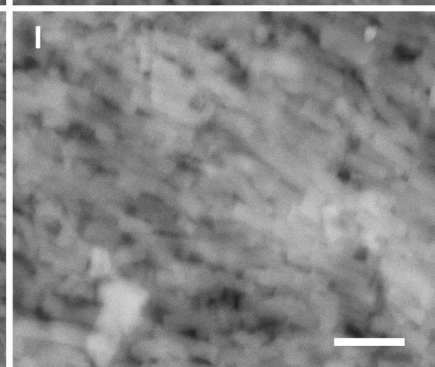
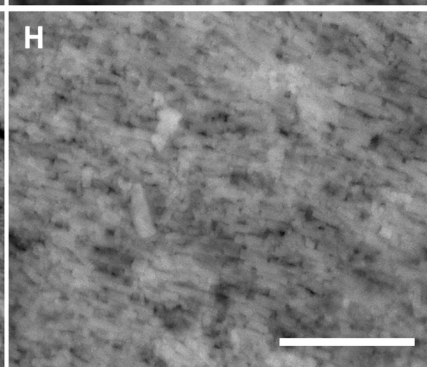
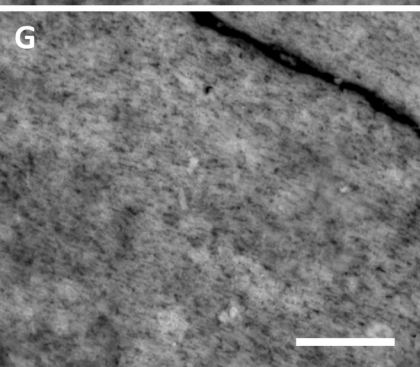
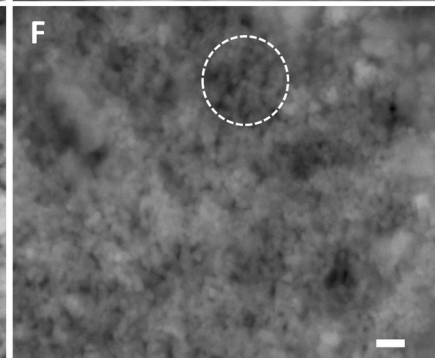
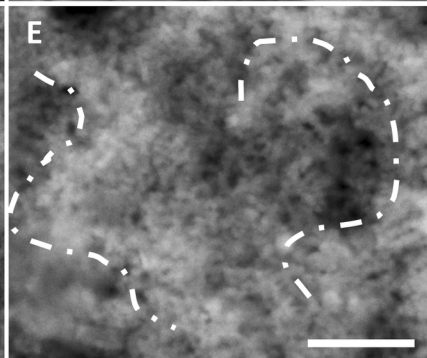
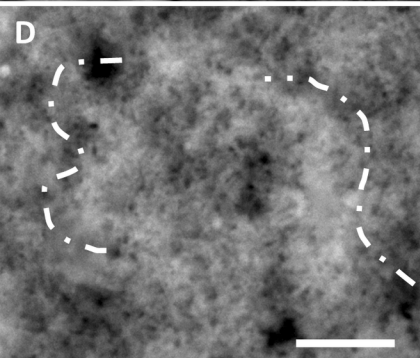
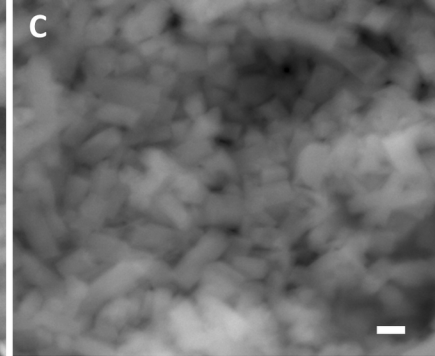
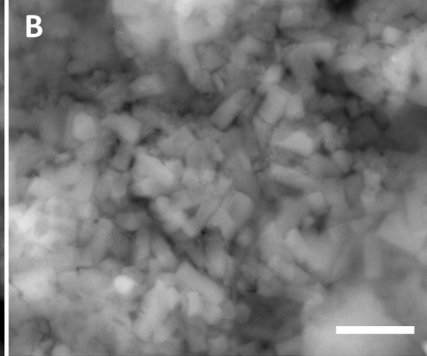
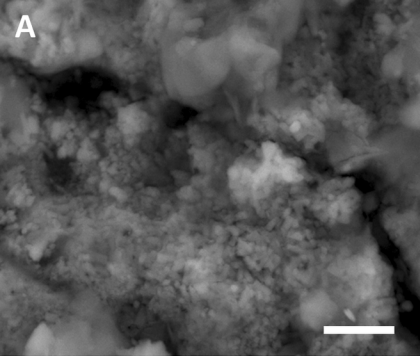


**Table 1.**

<b>Sample</b>	<b>Taxon</b>	<b>RAMAN</b>	<b>FTIR</b>	<b>MEB</b>
UBGD 30515	SPONGE	x		
UBGD 30617	SPONGE	x	x	x
UBGD 30618	SPONGE	x	x	
UBGD 30619	SPONGE	x	x	x
UBGD 30620	SPONGE			x
UBGD 30513	SPONGE	x	x	x
UBGD 30621	SPONGE		x	x
UBGD 30622	SPONGE	x	x	x
UBGD 30623*	SPONGE	x		x
UBGD 30624*	SPONGE	x		x
UBGD 30625	DISCINOID	x	x	x
UBGD 30626	DISCINOID	x	x	x
UBGD 30627	DISCINOID		x	
UBGD 30628	DISCINOID			x
UBGD 30629	DISCINOID		x	x
UBGD 30630	DISCINOID	x	x	
UBGD 30631	DISCINOID	x	x	x
UBGD 30632	DISCINOID	x	x	x
UBGD 30633*	DISCINOID	x		
UBGD 30634*	DISCINOID	x		
UBGD 30635	SHRIMP	x	x	x
UBGD 30636	SHRIMP	x	x	x
UBGD 30637	SHRIMP	x	x	x
UBGD 30638	SHRIMP	x	x	x
UBGD 30639*	SHRIMP	x		
UBGD 30640	LINGULOID	x	x	x
UBGD 30641	LINGULOID	x	x	x
UBGD 30642*	LINGULOID			x
UBGD 30643*	LINGULOID	x		

**Table 2.**

<b>Band</b>	<b>Raman shift (cm<sup>-1</sup>)</b>	<b>Interpretation</b>
<b>1</b>	420-430; $\nu_2\text{PO}_4^{3-}$	Doubly degenerate bending modes of O-P-O
<b>2</b>	~570-600; $\nu_4\text{PO}_4^{3-}$	Triply degenerate bending modes of O-P-O
<b>3</b>	~940; $\nu_1\text{PO}_4^{3-}$	Symmetric stretching modes of P-O
<b>4</b>	~1017; $\nu_3\text{PO}_4^{3-}$	Triply asymmetric stretching modes of O-P-O